



## Amorphous low-coordinated cobalt sulphide nanosheet electrode for electrochemically synthesizing hydrogen peroxide in acid media

Zhenglin Chen<sup>a</sup>, Guangzhen Liu<sup>b</sup>, Wenjing Cao<sup>b</sup>, Lixia Yang<sup>b,\*</sup>, Longshuai Zhang<sup>b</sup>, Shuqu Zhang<sup>b</sup>, Jianping Zou<sup>b</sup>, Renjie Song<sup>b</sup>, Wenhong Fan<sup>a</sup>, Shenglian Luo<sup>a,b,\*</sup>, Dionysios D. Dionysiou<sup>c</sup>

<sup>a</sup> School of Space and Environment, Beihang University, Beijing 100191, PR China

<sup>b</sup> Key Laboratory of Jiangxi Province for Persistent Pollutants Control and Resources Recycle, Nanchang Hangkong University, Nanchang 330063, PR China

<sup>c</sup> Environmental Engineering and Science Program, Department of Chemical and Environmental Engineering, University of Cincinnati, Cincinnati, OH 45221, USA



### ARTICLE INFO

#### Keywords:

Low-coordination  
 $\text{H}_2\text{O}_2$   
 $2\text{e}^-$  oxygen reduction reaction  
 $\text{CoS}_x$   
Amorphous

### ABSTRACT

This study investigates in-depth the local atomic environment-property relationship of amorphous low-coordination catalysts toward the  $2\text{e}^-$  oxygen reduction reaction (ORR). Here, an ethanol-assisted slow nucleation strategy was adopted to flexibly regulate the intrinsic activity of  $\text{CoS}_x$  nanostructures for efficient  $2\text{e}^-$  ORR by oriented control the coordination number of Co. When Co and S form  $\text{Co-S}_4$  coordination structures, the  $\text{CuNW}@\text{CoS}_4$  exhibits an ultra-low overpotential (0.018 V) with 93 %  $\text{H}_2\text{O}_2$  selectivity, and 91 % Faraday efficiency in acidic media at 0.1 V<sub>RHE</sub>. Furthermore, thus produced  $\text{H}_2\text{O}_2$  satisfies in-situ organic pollutants degradation by electro-Fenton. XAS and DFT calculations unveil the S-induced forming of abundant low-coordinated Co atoms as active sites in  $\text{Co-S}_4$ , validating that a favorable d-band energy level of Co center can weaken the  $\text{OOH}^*$  adsorption for accelerating the  $\text{H}_2\text{O}_2$  production kinetics. This work is anticipated to enlighten the rational design of high-performance ORR catalysts for practically feasible  $\text{H}_2\text{O}_2$  electrosynthesis toward wastewater remediation.

### 1. Introduction

Hydrogen peroxide ( $\text{H}_2\text{O}_2$ ) is a high-value, environmentally friendly oxidant, and is widely utilized in the chemical industry and environmental remediation [1]. The U.S. Environmental Protection Agency listed  $\text{H}_2\text{O}_2$  as an important disinfectant for confronting the COVID-19 pandemic [2]. The current industrial manufacturing of  $\text{H}_2\text{O}_2$  involves an energy-intensive anthraquinone redox process that was first developed by Riedl and Pfleiderer in 1939 [3]. This process, despite enabling the large production of high concentrations of  $\text{H}_2\text{O}_2$ , is considered not green since the complex and large scale infrastructure is required while creating intensive waste. Notably, the centralized  $\text{H}_2\text{O}_2$  production meets the demands of large-scale industrial applications, but for many distributed applications (e.g. water treatment), only less than 1000 ppm (29 mM) of  $\text{H}_2\text{O}_2$  is sufficient [4]. This motivated the exploration of alternative methods for the on-site and on-demand production of  $\text{H}_2\text{O}_2$ , allowing many applications to be practicable, such as the Electro-Fenton

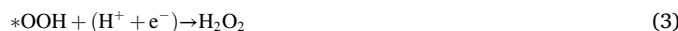
(EF) process.

Electrochemical synthesis of  $\text{H}_2\text{O}_2$  via the two-electron oxygen reduction reaction ( $2\text{e}^-$  ORR) provides a more sustainable solution for distributed utilization [5,6]. Massive efforts were conducted on developing  $2\text{e}^-$  ORR electrocatalysts in alkaline solutions due to the fast kinetic rate and easily achievable high selectivity [7,8]. Nevertheless, the production of  $\text{H}_2\text{O}_2$  in alkaline media faces the following drawbacks: (i)  $\text{H}_2\text{O}_2$  is deprotonated ( $\text{pK}_a > 11$ ) and tends to decompose, requiring to be used immediately [9]; (ii) Stabilizers (e.g. phosphoric acid) is required to retard  $\text{H}_2\text{O}_2$  decomposition, which increases operating costs [10]; (iii) Reactors based on alkaline membrane electrode assemblies (MEA) suffer from poor membrane stability and low activity [11]. As an alternative, making  $\text{H}_2\text{O}_2$  in acidic media can avoid these problems. Particularly, different from that in alkaline media,  $\text{H}_2\text{O}_2$  has a higher oxidation ability in acidic media, which makes  $\text{H}_2\text{O}_2$  workable and effective in wide applications like the typical Fenton process for wastewater treatment [12]. However, regarding conventional

\* Corresponding authors at: Key Laboratory of Jiangxi Province for Persistent Pollutants Control and Resources Recycle, Nanchang Hangkong University, Nanchang 330063, PR China.

E-mail addresses: [yanglixia829@163.com](mailto:yanglixia829@163.com) (L. Yang), [sllou@hnu.edu.cn](mailto:sllou@hnu.edu.cn) (S. Luo).

metal-based catalysts, corrosion and leaching occurred at high overpotentials always result in declined activity, and low selectivity is another downside [13]. Consequently, robust 2e<sup>-</sup> ORR electrocatalysts with outstanding selectivity and activity in acidic media are the basic factors for high yield and continuous generation of H<sub>2</sub>O<sub>2</sub>. Theoretically, the 2e<sup>-</sup> ORR selectivity is highly dependent on the adsorption free energy of the intermediate (OOH<sup>\*</sup>) on the catalyst [14]. A strong binding between \*OOH and catalytic centers causes the break of the O-O bond in OOH<sup>\*</sup>, enabling the formation of the reduced product, H<sub>2</sub>O. Conversely, the weak binding of \*OOH helps to preserve the O-O bond, favoring the production of H<sub>2</sub>O<sub>2</sub>, as shown in Eqs. (1) - (3) [15].



Undoubtedly, the selectivity of H<sub>2</sub>O<sub>2</sub> is tightly related to the oxygen binding strength ( $\Delta E_o$ ) of the oxygen molecule on the active centers [16,17]. Noble metals containing electrocatalysts like Pd- and Pt-alloys demonstrate remarkable selectivity and stability for 2e<sup>-</sup> ORR in acidic solutions because of the appropriate  $\Delta E_o$  there [18–20]. However, the high price restrains their wide practical applications. Some economical catalysts, especially carbon materials, have been proven as ideal acid catalysts, but on which the slow ORR kinetic rate brings about unwanted overpotential (> 300 mV) to initiate the generation of H<sub>2</sub>O<sub>2</sub>. That could damage the stability of carbon-based metal catalysts [21]. As it is difficult to achieve exceptional 2e<sup>-</sup> ORR selectivity and stability in both ways, constructing feasible reaction systems for on-site production of H<sub>2</sub>O<sub>2</sub> in acidic media remains in predicament [22–25].

Defect engineering is an important approach for modulating the electronic properties of electrocatalysts [26]. By creating defects in the catalyst, the average coordination numbers (ACN) of the metal atoms can be reduced, thereby tuning the energy in the d-band center, accompanied by regulated bond strength between the adsorbed oxygen intermediate and the metal surface, which is a flexible and feasible strategy for the 2e<sup>-</sup> ORR [27,28]. Amorphous transition metal-based catalysts applied in 2e<sup>-</sup> ORR have been receiving increasing attention, like those consisting of Co, Ni, Fe, Mo, etc., which are rich in d-orbital electronic states, abundant defects, and have appealing ORR activity [29–37]. For instance, Menezes et al. flexibly regulated the adsorption energy of \*OOH on Ni through a partial defect engineering strategy and achieved over 90 % 2e<sup>-</sup> ORR selectivity by adjusting the ACN of Ni atom [38]. Above findings reveal that tailoring the ACN of amorphous transition metal-based catalysts is available for optimizing  $\Delta E_o$  to achieve desired 2e<sup>-</sup> ORR selectivity and high stability.

Herein, a novel three-dimensional (3D) amorphous low-coordination electrode, CuNW@tCoSx, was developed as an effective activator to initiate the ORR, demonstrating a 93 % (0.1 V<sub>RHE</sub>) 2e<sup>-</sup> ORR selectivity and excellent stability in acidic media. Benefiting from the effective electron transport between the highly conductive Cu nanowire substrate and the amorphous CoSx, only 0.1 V<sub>RHE</sub> is required to trigger the reaction system, which is far below the redox potential of the active metal Co ( $\varphi^0 (Co^{3+}/Co^{2+}) = -0.28$  V). As a result, the Co active centers on CuNW@tCoSx are durable, even undergoing long-term runs (5 h) in acidic media, which maintains 99 % of the initial current and up to 91 % Faraday efficiency at the end of the test. When applied in a dual-chamber PEM/EF system, the CuNW@tCoSx electrode produces countless H<sub>2</sub>O<sub>2</sub> molecules to oxidize the adsorbed organic contaminants, shedding light on its promising potential in contamination removal. X-ray photoelectron spectroscopy (XPS) and X-ray absorption spectra (XAS) analysis proves that the oxidation defect state of Co atoms in CoSx is optimal when the ACN of S is four (ACN = 4). Namely, a central Co atom holds 4 S atoms as its nearest neighbors, therefore the structure is labeled as [CoS<sub>4</sub>]. Experimental and density functional theory (DFT) calculations reveal that the appropriate d-band energy level (Ed) of

[CoS<sub>4</sub>] optimizes the Gibbs adsorption free energy of intermediate \*OOH on Co, which greatly reduces the H<sub>2</sub>O<sub>2</sub> evolution overpotential and promotes the 2e<sup>-</sup> ORR kinetic rate. The unique amorphous CuNW@tCoSx electrode demonstrates high selectivity of 2e<sup>-</sup> ORR and outstanding stability in acidic media, outperforming most reported acidic electrodes, which tackles the thorny problems associated with acidic oxygen reduction reactions and meets the demand for distributed applications in the EF treatment of wastewater.

## 2. Experimental section

### 2.1. Fabrication of CuNW on Cu foam

Firstly, Cu(OH)<sub>2</sub> nanowires (NW) were synthesized through a chemical oxidation method, and a typical process was as follows: Cu foam with a size of 2 × 3 cm<sup>2</sup> were cleaned with hydrochloric acid (37 %) and then sonicated in ethanol, acetone and deionised water for 10 min. The cleaned Cu foam was then immersed into 80 mL of a solution containing 2.0 M NaOH and 0.125 M (NH<sub>4</sub>)<sub>2</sub>S<sub>2</sub>O<sub>8</sub> for 20 min. Eventually, the Cu foam bearing Cu(OH)<sub>2</sub> NW with a light blue color was taken out from the solution, rinsed with deionized water, and dried in air. Afterward, the prepared Cu(OH)<sub>2</sub> NW were calcined at 180 °C in the air for 1 h to obtain CuO NW and calcined at 300 °C in the H<sub>2</sub>/Ar (5 %/95 %) for 1 h to obtain Cu NW.

### 2.2. Fabrication of amorphous CoSx on CuNW (CuNW@tCoSx)

CoSx was grown on CuNW via the chronoamperometric method using a three-electrode configuration with CuNW (2 × 3 cm<sup>2</sup>), Pt mesh, and Ag/AgCl as working electrode, counter electrode, and reference electrode, respectively. The electrodeposition electrolyte an ethanol-water solution with a volume ratio of 2:8, containing 0.1 M cobalt nitrate hexahydrate and 0.5 M thiourea. The electrodeposition of CoSx was conducted at –0.9 V vs Ag/AgCl, which lasted various minutes (t = 5, 8 and 11) to regulate the CoSx layer thickness. After that, CuNW@tCoSx was washed with water and ethanol, followed by being dried at 60 °C for 4 h. Finally, CuNW@tCoSx was successfully obtained by calcination in Ar gas at 300 °C for 1 h.

### 2.3. Characterization

The details of transmission electron microscopy (TEM), field emission scanning electron microscopy (FESEM), X-ray diffraction (XRD), X-ray photoelectron spectroscopy (XPS), inductively coupled plasma atomic emission spectrometer (ICP-OES), electron paramagnetic resonance (EPR) spectrometer, Raman spectrometer, X-ray absorption fine structure spectra (XAFS), and the details are provided in the [Supporting Information \(Text S2\)](#).

### 2.4. Analysis methods

The concentrations of contaminants [sulfamethoxazole (SMX), flufenicol (FLO), ciprofloxacin (CIP), p-chlorophenol (4-CP) and bisphenol A (BPA)] were monitored by a high-pressure liquid chromatographer (HPLC Shimadzu LC-20AD, Tokyo, Japan) with a TC-C18 reverse-phase column (150 mm × 4.6 mm, 5 μm, Agilent). The detailed testing conditions were provided in [Table S7](#). Detection of •OH production using EPR with DMPO as the spin trapping agent.

### 2.5. Electrochemical evaluation

The ORR performances were evaluated with a CHI760E Electrochemical Workstation (CH Instruments) using a three-electrode configuration electrochemical cell. The Ag/AgCl electrode and graphite rod were used as the reference electrode and counter electrode, respectively. The rotating ring disk electrode (RRDE, American Pine Instruments, disk

area: 0.2475 cm<sup>2</sup>, ring area: 0.1866 cm<sup>2</sup>, theoretical collection efficiency (N) of 37 %) was employed as the work electrode, and the detailed test procedure is provided in [Text S4](#). Correction of all recorded potentials to the reversible hydrogen electrode (RHE) using the following equation:

$$E_{\text{RHE}} = E_{\text{Ag/AgCl}} + 0.197 + 0.0592 \times \text{pH} \quad (4)$$

$$E_{\text{Ag/AgCl}} = E_{\text{RHE}} - 0.2224 - 0.05916 \times \text{pH} \quad (5)$$

The electron transfer number (n) was calculated as follows:

$$n = \frac{4I_d}{I_d + I_r/N} \quad (6)$$

The H<sub>2</sub>O<sub>2</sub> selectivity was calculated as follows:

$$\text{H}_2\text{O}_2 \text{ selectivity}(\%) = \frac{200 \times I_r}{N} / (I_d + I_r / N) \quad (7)$$

Where I<sub>d</sub> is the disk current; I<sub>r</sub> is the ring current; N = 0.37.

The Tafel slopes were calculated according to the Tafel equation  $\eta = b \log(j/j_0)$  based on the LSV curves, where  $\eta$  is the overpotential, b is the Tafel slope, j is the current density, and  $j_0$  is the exchange current density.

Electrochemical impedance spectra (EIS) data were collected with frequencies ranging from 10<sup>5</sup> to 10<sup>-2</sup> Hz at the open circuit potential of 5.0 mV. Electrochemical capacitance measurements were achieved from double-layer charging curves using the cyclic voltammograms (CVs) at the potential window of 0.05–0.15 V vs. Ag/AgCl in 0.1 M Na<sub>2</sub>SO<sub>4</sub> solution. The detailed information is provided in [Text S4 in SI](#).

## 2.6. H<sub>2</sub>O<sub>2</sub> concentration measurement

The yield of H<sub>2</sub>O<sub>2</sub> was determined by the Ce(SO<sub>4</sub>)<sub>2</sub> titration method. The conversion of yellow Ce<sup>4+</sup> to colorless Ce<sup>3+</sup> after addition of H<sub>2</sub>O<sub>2</sub> based on the following reaction:



The calibration curve fitting equation for UV-Vis (317 nm) absorbance of Ce(SO<sub>4</sub>)<sub>2</sub> solution was acquired ( $y = 5.38,657x - 0.00,804$ ,  $R^2 = 0.9998$ ). The calculation procedure of the Faraday efficiency (H<sub>2</sub>O<sub>2</sub>, EF %) of the dual chamber PEM is provided in [Text S4 in SI](#).

## 2.7. DFT calculation

All the density functional theory (DFT) calculations were conducted with the Vienna Ab initio Simulation Package (VASP). The spin had been considered. The generalized gradient approximation (GGA) and Perdew-Burke-Ernzerhof (PBE) formulation were adopted to describe the exchange correlation energies. The projector augmented wave (PAW) method was used to describe the ionic cores, and valence electrons were considered using a plane wave basis with a kinetic energy cutoff of 450 eV. Partial occupancies of the Kohn-Sham orbitals were allowed using the Gaussian smearing method with a width of 0.05 eV. The electronic energy was considered self-consistent when the energy change was smaller than 10<sup>-5</sup> eV. The convergence criterion of geometry relaxation was smaller than 0.05 eV Å<sup>-1</sup>. The Brillouin zones (BZ) were sampled by using the surfaces structures of 2 × 2 × 1 Monkhorst-Pack K-point.

The free energy (ΔG) for elemental reaction step were calculated as:

$$\Delta G = \Delta E + \Delta E ZPE - T \Delta S \quad (9)$$

Where ΔE is the difference between the total energy, ΔE ZPE and ΔS are the differences in the zero-point energy and the change of entropy, T is the temperature (T = 300 K in this work), respectively. The U correction had been adopted in our systems for Co atoms d states.

## 2.8. Degradation of organic contaminants

The degradation experiments were carried out using a 100 mL dual-chamber proton exchange membrane (PEM)/EF reactor (0.1 M Na<sub>2</sub>SO<sub>4</sub> electrolyte with pH 5.0). During each test, 2 mM Fe<sup>2+</sup> and 10 mg L<sup>-1</sup> organic pollutants [sulfamethoxazole (SMX), florfenicol (FLO), ciprofloxacin (CIF), p-chlorophenol (4-CP) and bisphenol A (BPA)] were added into the cell; O<sub>2</sub> was aerated into the solution at a flow rate of 0.4 L min<sup>-1</sup>. The CuNW@tCoSx foam worked as the working electrode (2 × 3 cm<sup>2</sup>). The anode chamber was equipped with a Pt mesh (1.5 cm × 1.5 cm) as the counter electrode and Ag/AgCl as the reference electrode. A constant potential of 0.1 V<sub>RHE</sub> (≈ -0.4 V vs Ag/AgCl) was applied to initiate the degradation process. For visible light comparison experiments, the 300 W Xenon arc lamp (Microsolar300, Beijing Perfectlight) was used to supply the visible light, and was about 10 cm away from the solution surface. At predetermined intervals, a 1.0 mL aliquot was sampled, filtered through a 0.22 μm membrane, and immediately injected into a vial with 0.5 mL methanol for further analysis.

## 3. Results and discussion

### 3.1. Construction of CuNW@tCoSx and structural characterization

The construction process of the CuNW@tCoSx electrode is illustrated in [Fig. 1a](#) (x represents the number of S atoms around a single Co atom, and t is the electrodeposition time for CoSx). Cu(OH)<sub>2</sub> nanowires (NW) were first grown on Cu foam in a solution containing sodium hydroxide (NaOH) and ammonium persulfate [(NH<sub>4</sub>)<sub>2</sub>S<sub>2</sub>O<sub>8</sub>], then calcined in air to form CuO NW, followed by reducing CuO to Cu with H<sub>2</sub> at 300 °C. Afterwards, CoSx nanosheets were electrodeposited on Cu NW in an electrolyte consisting of ethanol (C<sub>2</sub>H<sub>5</sub>OH), H<sub>2</sub>O, cobalt nitrate hexahydrate (Co(NO<sub>3</sub>)<sub>2</sub>·6 H<sub>2</sub>O), and thiourea (CH<sub>4</sub>N<sub>2</sub>S). As the conductivity of the organic solution is low, CoSx nuclei slowly grow and assemble in amorphous nanosheets along the Cu NW surface. The Cu foam bearing CuNW and CoSx was then annealed in an Ar atmosphere at 300 °C to remove the crystalline water in CoSx to obtain the target CuNW@CoSx electrode ([Fig. S1](#)). The resulting electrodes are specifically labeled as CuNW@tCoSx. According to the controlled experiments, 5, 8, and 11 min are selected. The SEM images of the CuO NWs at different magnifications ([Fig. 1b](#) and [Fig. S2](#)) show that dense and uniform CuO NW are well aligned on the Cu foam, which turns into curled Cu NW after being reduced by H<sub>2</sub> ([Fig. 1c](#) and [Fig. S3](#)). [Fig. 1d](#) displays an obvious core-shell structure of CuNW@8CoSx with Cu NW as the core and CoSx as the shell. Every conductive Cu NW is completely wrapped by small, thin, and intercrossed CoSx nanosheets ([Fig. 1e](#)). And the CoSx shell thickens with prolonged electrodeposition duration ([Figs. S4, S5, and S6](#)). The TEM image of CuNW@8CoSx further reveals the assembling way of CoSx on Cu NW. It looks like the out-stretched CoSx nanosheets grow from the Cu substrate, building a "stem-leaf" structure ([Fig. 1f](#)). This is an advantageous construction for electrocatalysis. When applied in the electrochemical reaction, the Cu stem can work as a highway for directionally transporting charges to the 3D CoSx shell enriched with numerous active sites. The energy dispersive X-ray spectroscopy (EDX) identifies the elements including Cu, Co, and S ([Fig. S7](#)), which are uniformly distributed over a single CuNW@8CoSx, as observed from the element mapping images ([Fig. 1g](#)). The corresponding figures of Cu, Co, and S demonstrate that Cu NW is the skeleton, and Co and S atoms seem everywhere along the Cu NW and CoSx. The crystal structure of CuO NW, Cu NW, and CuNW@tCoSx are revealed by the x-ray diffraction (XRD) characterization ([Fig. S8](#)). Since the specific peaks assigned to Cu are intense, those indexed to CuO are nearly invisible. But the amplified parts of the XRD patterns validate the disappearance of CuO (JCPDS No. 80-1917), proving the reduction of CuO to Cu. As for the CuNW@tCoSx, no peaks associated with CoSx are detectable, indicating the amorphous nature of CoSx nanosheets (NS). Furthermore, shown as the images in [Fig. 1h](#) and [Fig. 1i](#), the bright round patch in the

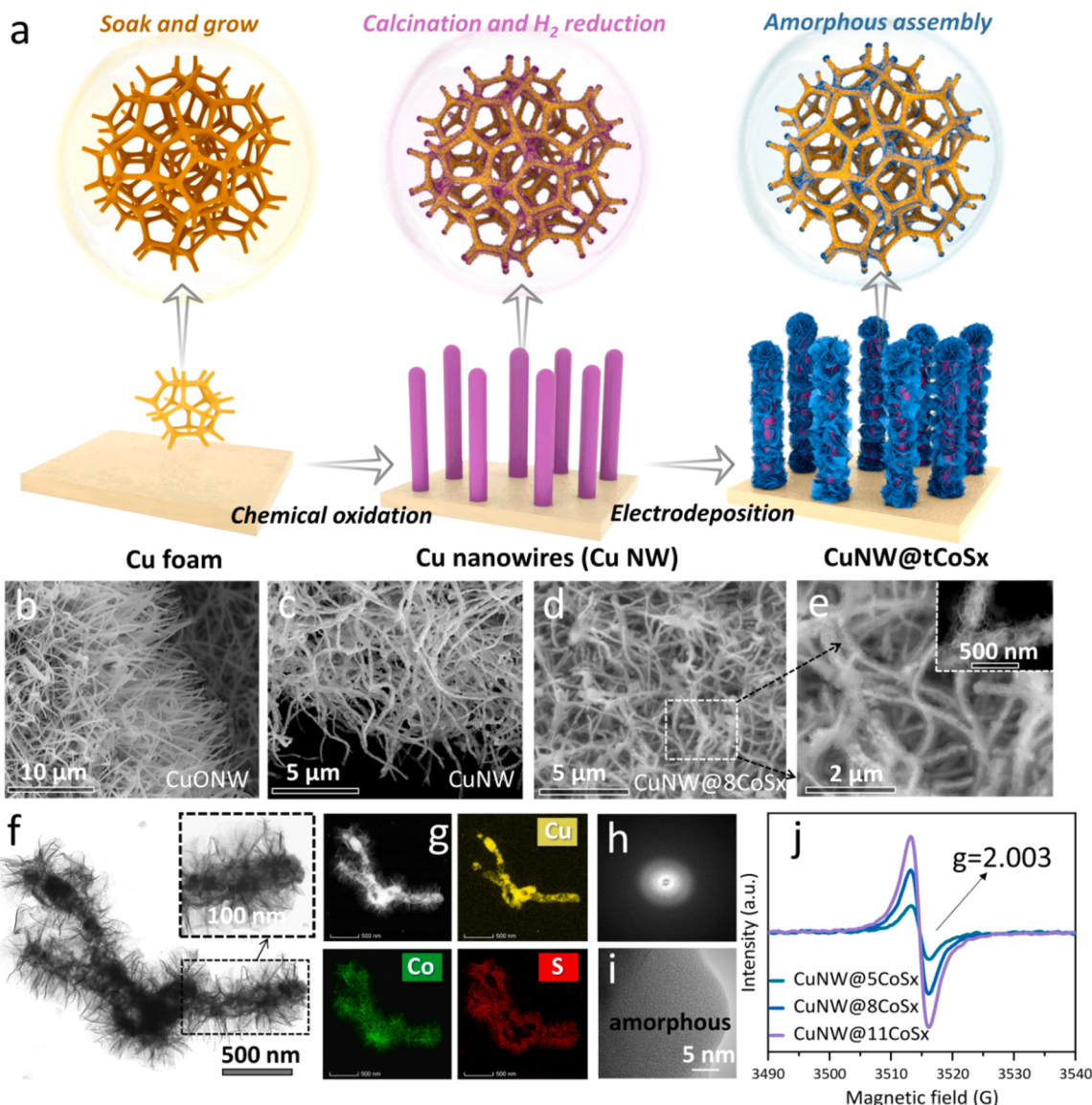


**Fig. 1.** (a) Schematic synthesis of CuNW@tCoSx electrodes on copper foam (CF). (b) SEM image of CuONW. (c) SEM image of Cu NW. SEM image of CuNW@ 8CoSx at (d) low and (e) high magnification. (f) TEM image, (g) element mapping, (h) SAED pattern, (i) HRTEM image of CuNW@ 8CoSx. (j) EPR spectra of CuNW@tCoSx ( $t = 5, 8$ , and  $11$ ) candidates.

SAED pattern and the HRTEM image of CoSx nanosheets collected from CuNW@ 8CoSx evidence the amorphous structure as well. Since no long-range ordered lattice fringes associated with CoSx are observed in the whole HRTEM image (Fig. S9). Generally, amorphous materials are filled with defects containing point defects [39], surface defects [40], and lattice defects [41], which can be unveiled by electron paramagnetic resonance (EPR) spectroscopy. As Fig. 1j displays, CuNW@tCoSx candidates ( $t: 5, 8, 11$ ) exhibit strong EPR signals at  $g = 2.003$ , which can be attributed to the electrons trapped in the S vacancies (Vs) near the Co atoms [42], and the intensity rises with thickened CoSx shell. The phase composition and structural defects in CuNW@tCoSx are further analyzed with Raman spectroscopy (Fig. S10). Those peaks located at wave numbers below  $300 \text{ cm}^{-1}$  are assigned to Co<sub>9</sub>S<sub>8</sub>, and the other peaks are labeled as E<sub>g</sub>, F<sub>2g</sub>, and A<sub>1g</sub> modes of CoS, respectively [43,44]. Additionally, the A<sub>1g</sub> peak negatively shifts to the lower wave number and its intensity reduces with growing CoSx content, which is primarily ascribed to the growing Vs numbers. That's to say, the S atom number held by a Co atom lessens, expressed as the coordination number between Co and S minimizes [45].

### 3.2. Atomic and electronic structure of CuNW@tCoSx

As the XPS spectra of Cu NW in Fig. 2a show, except for the specific peaks indexed to Cu<sup>0</sup>, the binding energies (BE) of 934.27 eV and 954.19 eV are assigned to the Cu 2p<sub>3/2</sub> electron and Cu 2p<sub>1/2</sub> electron, which come from the residual Cu<sup>2+</sup> ions in Cu NW [46]. After CoSx loaded, no Cu<sup>2+</sup> is identified, for Cu<sup>2+</sup> ions were utterly reduced in Cu<sup>0</sup> during the electrodeposition process. Notably, compared with Cu NW, a positive shift of 0.3 eV related to the Cu<sup>0</sup> (932.51 and 952.60 eV) in CuNW@ 8CoSx appears, indicating the electron density around Cu<sup>0</sup> decreases due to the high electronegativity of S atoms. Besides, the BE of Co<sup>3+</sup> 2p<sub>3/2</sub> electron in CuNW@ 5CoSx is 780.05 eV, which is 780.45 eV in CuNW@ 8CoSx, 780.55 eV in CuNW@ 11CoSx, increased by 0.4 eV and 0.5 eV, accordingly (Fig. 2b). Furthermore, taking the BE of S 2p (S<sup>x-</sup> 2p<sub>3/2</sub>) in CuNW@ 5CoSx as a reference, the BE decreases by 0.1 eV in CuNW@ 8CoSx, and 0.4 eV in CuNW@ 11CoSx (Fig. 2c). With more CoSx deposited, the conversely chemical shifts between S and Co illustrate a fact that electrons from Co migrating to S, which suggestss the chemical environment around Co atoms changes due to S [47]. Based on the contents of S and Co determined by XPS, the molar ratio of S<sup>x-</sup> to

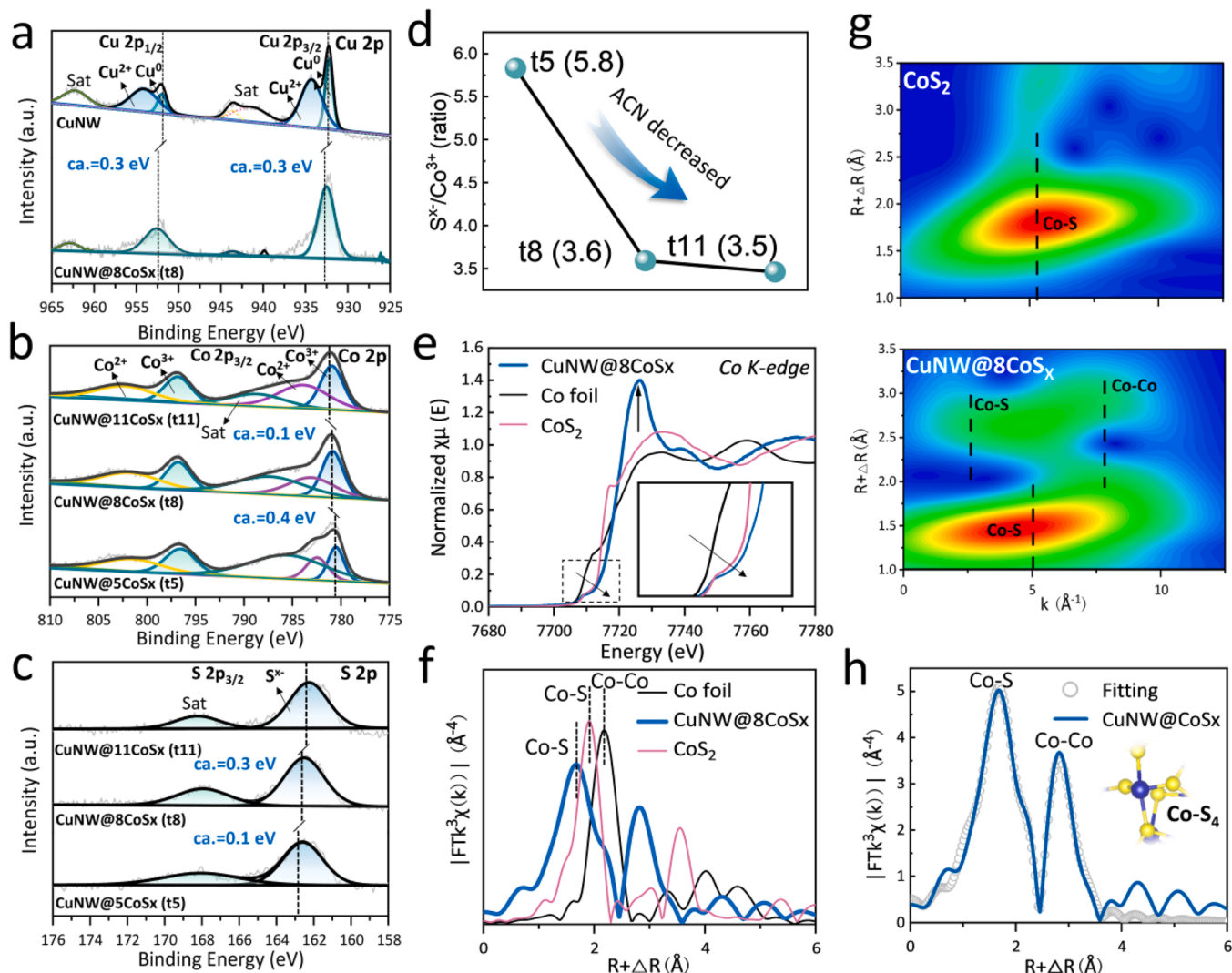


**Fig. 2.** (a) XPS spectra of Cu 2p in CuNW and CuNW@ 8CoSx. (b) Co 2p, (c) S 2p XPS spectra, and (d) average coordination environment (ACN) of Co based on  $Sx^-/Co^{3+}$  ratio of CuNW@tCoSx ( $t = 5, 8$ , and  $11$ ). (e) Co K-edge XANES, (f) EXAFS, (g) WT-EXAFS patterns, and (h) EXAFS fitting of CuNW@ 8CoSx and references.

$Co^{3+}$  was calculated to assess the average numbers of S atoms that coordinate with a Co atom (ACN). As exhibited in Fig. 2d and Table S2, the ACN of Co is ranked as t5 (5.8) > t8 (3.6) > t11 (3.5). The chemical environment and electronic state of Co sites in CoSx NS are successfully tailored by controlling the electrodeposition process.

The Co K edge X-ray absorption near-edge structure (XANES) spectra demonstrate that the absorption edge of CoSx in CuNW@ 8CoSx is higher than perfect  $CoS_2$  (Actually, six S atoms surround a Co atom, the ACN is 6) and Co foil, indicating an increase in the valence state of Co due to the formation of the amorphous state (Fig. 2e), which is consistent with the XPS results [48]. Compared to perfect  $CoS_2$  and Co foil, CuNW@ 8CoSx exhibits a stronger white line peak, implying a lower coordination symmetry and coordination number for Co [49]. The Fourier transform (FT)  $k^3$ -weighted EXAFS spectrum of the Co K edge displays two main peaks, one at 1.53 Å corresponds to Co-S coordination, and the other at 2.78 Å is related to the Co-Co coordination shell (Fig. 2f) [50]. By referring to the FT-EXAFS feature of perfect  $CoS_2$ , the specific peak of Co-S in CuNW@ 8CoSx shifts to lower R-space, which suggests the shrunk crystal lattice of CoSx caused by a large number of Vs [51]. Furthermore, the reduced R-space amplitude of CoSx clarifies the abated S numbers circling the Co atom and higher mean-square disorder [52], confirming the presence of plentiful S vacancies as well. And the local coordination environment (Fig. 2g) was visually

determined with wavelet transform (WT) analysis. As shown, the Co-S in CuNW@ 8CoSx peak is at 5.0 Å<sup>-1</sup>, negatively shifts by 0.5 Å<sup>-1</sup> compared with the perfect  $CoS_2$ , further evidencing the crystal shrinkage of CoSx. Other two weak maxima are observed at 2.51 Å<sup>-1</sup> and 7.89 Å<sup>-1</sup> on CuNW@ 8CoSx, which results from the Co-S bonds in the second shell layer and Co-Co at the edges of CoSx, respectively [53]. Moreover, the coordination configuration of Co in CuNW@ 8CoSx was investigated using quantitative least squares EXAFS curve fitting analysis (Fig. 2h). The best-fit analysis finds out two main peaks at 1.53 Å and 2.78 Å (no phase shift), in agreement with the FT-EXAFS results, indicating that both the Co-S, and Co-Co coordination are present in the first shell layer of CoSx. The CN of Co, lengths of Co-S and Co-Co bond were calculated by EXAFS fitting (Table S3). The calculated S number held by a central Co atom is 3.8 in CuNW@ 8CoSx, confirming the ACN of Co atoms in CuNW@ 8CoSx is about four (CN≈4). Consequently, the CoSx here is described as  $[CoS_4]$ , which indicates a low coordination CoSx structure. This finding is in accordance with the conclusion based on XPS spectra (Fig. 2d).

### 3.3. Electrocatalytic oxygen reduction on CuNW@tCoSx

Electrochemical tests were conducted to evaluate the performance of CuNW@tCoSx in ORR. Cyclic voltammetric (CV) curves recorded on

CuNW@tCoSx and Cu NW (Fig. S11a) demonstrate that CuNW@ 8CoSx shows the most significant oxygen reduction current surge in the potential range from  $-0.2$  V to  $0.0$  V. And the CuNW@ 8CoSx presents a well-defined intense reduction peak in  $O_2$ -saturated solution while no ORR peak is obtained in the Ar-saturated solution (Fig. S11b). Of note, Cu NW is invalid over the entire scan voltage window due to the lack of active sites, confirming that CoSx provides the active catalytic interface for ORR. Moreover, the electrochemical impedance spectra (EIS) analysis concerning all the CuNW@tCoSx and Cu NW electrodes (Fig. S11c) shows that the charge transfer resistance on CuNW@ 8CoSx is the lowest, indicating the fastest electron transfer rate there. Derived from the CV curves (Fig. S11d-g), the largest electrochemical active surface areas (ECSA) is attained on CuNW@ 8CoSx, which is estimated by the double layer capacitance ( $C_{dl}$ ) calculated from the slope of the linear relationship between the current density against the scan rate. The CuNW@ 8CoSx present a  $C_{dl}$  of  $2.61 \text{ mF cm}^{-2}$ , almost 2.46 times that of

CuNW@ 11CoSx ( $1.06 \text{ mF cm}^{-2}$ ), 5.01 times that of CuNW@ 5CoSx ( $0.52 \text{ mF cm}^{-2}$ ) and 43.5 times that of CuNW ( $0.06 \text{ mF cm}^{-2}$ ) (Fig. S10h). It is believed that the appropriate loading and ACN of CoSx on CuNW@ 8CoSx account for the outstanding electrochemical capacity [54,55].

Additionally, a rotating ring-disk electrode (RRDE) technique was employed to monitor the  $2e^-$  ORR conducted on the CuNW@tCoSx and Cu NW electrodes in  $O_2$ -saturated electrolytes. All potentials were calibrated to reversible hydrogen electrode (RHE). The generated  $H_2O_2$  was quantified with a Pt ring electrode at  $1.3$  V [56]. As Fig. 3a depicts, the CuNW@ 8CoSx outperforms all the other electrodes by showing the highest diffusion-limiting ring current,  $0.368 \text{ mA}$  at  $0.1$  V, and the lowest Tafel slope,  $135 \text{ mV dec}^{-1}$  (Fig. 3b), which validates the fastest ORR kinetic rate on CuNW@ 8CoSx. The  $H_2O_2$  selectivity on Cu NW is only 23 %, much lower than those on CuNW@tCoSx electrodes, verifying the CoSx shell on Cu is responsible for the  $H_2O_2$  creation (Fig. S12).

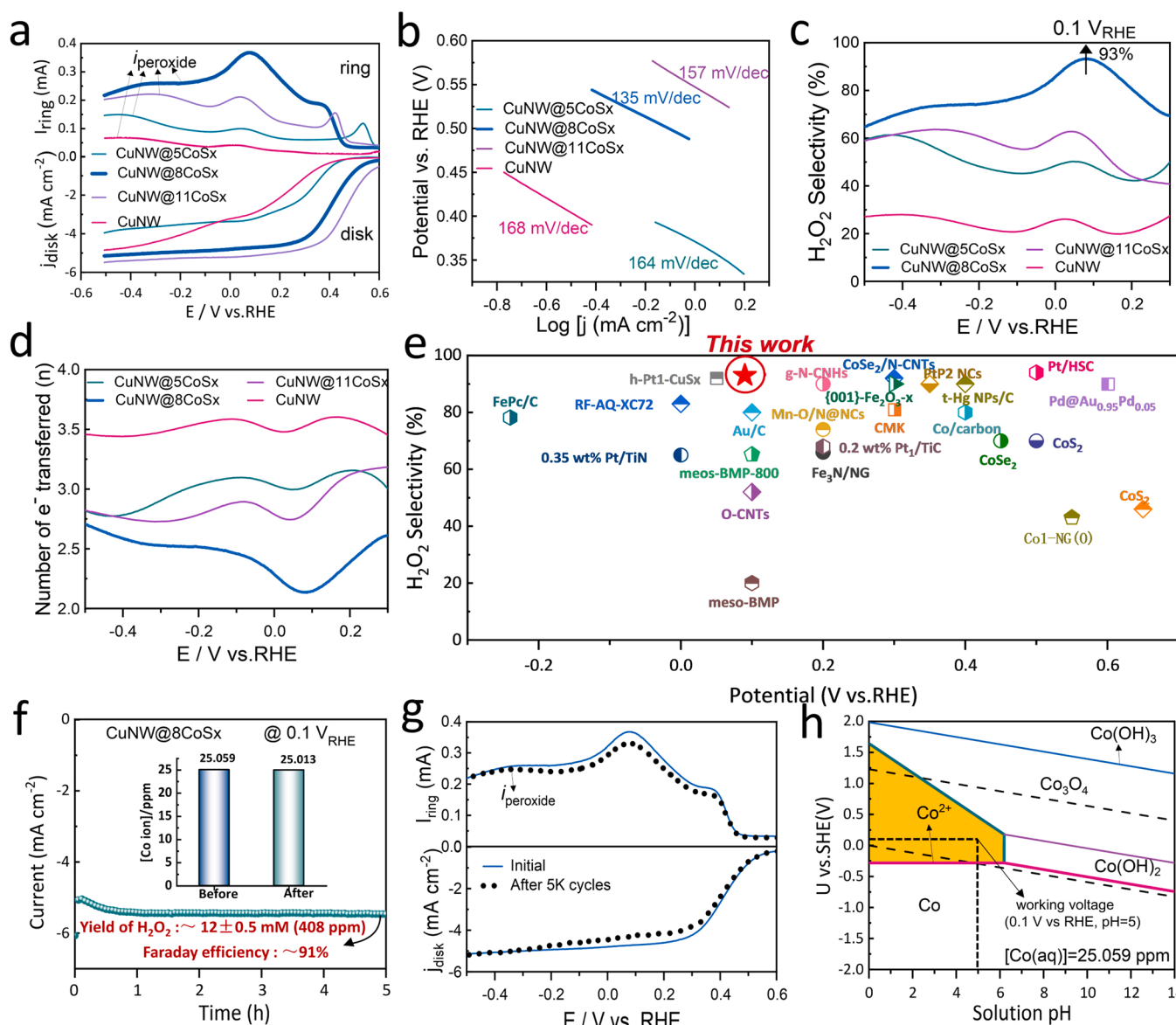


**Fig. 3.** (a) RRDE polarization curves at 1600 rpm in  $O_2$ -saturated  $0.1 \text{ M Na}_2\text{SO}_4$  (pH 5, 5 mV/s) with the ring current ( $I_{ring}$ ) shown in the upper part and disk current ( $j_{disk}$ ) in the lower part. (b) Tafel slope, (c) the calculated selectivity, and (d) the number of electrons transferred ( $n$ ) of CuNW@tCoSx ( $t = 5, 8$ , and  $11$ ) and CuNW. (e) comparison of the selectivity for  $H_2O_2$  electrosynthesis in acidic media on CuNW@ 8CoSx and other reported electrocatalysts. (f) chronoamperometry curve of  $H_2O_2$  production in  $O_2$ -saturated  $0.1 \text{ M Na}_2\text{SO}_4$  (pH 5) at  $0.1 \text{ V}$  vs RHE in an H-type electrochemical cell (Inset: ICP-OES results illustrating Co contents in CuNW@8CoSx before and after the reaction). (g) Comparison of RRDE polarization curves of CuNW@ 8CoSx before and after 5 K ADT cycles. (h) Pourbaix diagram of CuNW@ 8CoSx (Co ion).

In Fig. 3c, the calculated  $\text{H}_2\text{O}_2$  selectivity on  $\text{CuNW@8CoSx}$  approaches 93 % at 0.1 V. Notably, the electron transfer number only fluctuates between 2.1 and 2.3 (Fig. 3d), revealing a highly selective 2e<sup>-</sup> ORR pathway rendered by  $\text{CuNW@8CoSx}$ , which is superior to most reported acid catalysts such as monoatomic-, transition metal-, carbon-, and noble-metals based catalysts (Fig. 3e and Table S4). Furthermore, through comparison of 2e<sup>-</sup> ORR selectivity and  $\text{H}_2\text{O}_2$  yield with recently reported amorphous electrocatalysts, a conclusion can be drawn that  $\text{CuNW@8CoSx}$  is among the state-of-the-art amorphous electrocatalysts (Table S5). Besides, to validate the on-site production of  $\text{H}_2\text{O}_2$  in acidic media, the  $\text{H}_2\text{O}_2$  concentration was measured in 0.1 M  $\text{Na}_2\text{SO}_4$  at pH 5 by a traditional cerium sulfate  $\text{Ce}(\text{SO}_4)_2$  titration method (Electrochemical measurement, Supporting Information) [57]. As plotted in Fig. S13, an  $\text{H}_2\text{O}_2$  output of 85 ppm is achieved at 0.1 V within 30 min, which displays the feasibility of  $\text{CuNW@8CoSx}$  as an efficient electrode for  $\text{H}_2\text{O}_2$  production.

The stability of the favorable 2e<sup>-</sup> ORR and the consecutive  $\text{H}_2\text{O}_2$  operating current are indispensable features in practical applications [58]. Therefore, the long-term stability of  $\text{CuNW@8CoSx}$  was tested with chronoamperometry at 0.1 V, 0.1 M  $\text{Na}_2\text{SO}_4$ , pH 5) for 5 h in an

H-type electrochemical cell (Fig. S14). After the prolonged operation, about 99 % of the initial current is retained, validating the exceptional durability (Fig. 3 f). The quantification result shows that the  $\text{H}_2\text{O}_2$  Faradaic efficiency (FE) is high up to 91 %, and 408 ppm of  $\text{H}_2\text{O}_2$  is produced within 5 h. In addition, the ICP-OES analysis demonstrates that only 0.046 ppm of Co ions leach (Table S1 and Fig. 3 f) over the test duration, indicating its remarkable physical stability. Moreover, accelerated degradation tests (ADT) were performed to disclose the stability regarding the transfer behaviors of electrons on  $\text{CuNW@8CoSx}$ . As illustrated in Fig. 3 g, even after 5 K (5000) ADT cycles, the losses in both ring and disk current are negligible. Meanwhile, the well-preserved  $\text{H}_2\text{O}_2$  selectivity (92 %) and electron transfer number for  $\text{CuNW@8CoSx}$  approve the steady electron transfer pathway and active sites in the nanoscale (Fig. S15). Moreover, the XRD pattern of  $\text{CuNW@8CoSx}$  remains unchanged after the long reaction (Fig. S16a). SEM and TEM results also confirm that the amorphous structure of the 3D nanosheets of  $\text{CuNW@8CoSx}$  electrode keeps constant, which verifies its high structural stability (Fig. S16b-e). The EDS analysis of the elemental composition in the used  $\text{CuNW@8CoSx}$  is the same as the fresh one (Fig. S16f-i). The Pourbaix diagram calculated based on the actual Co

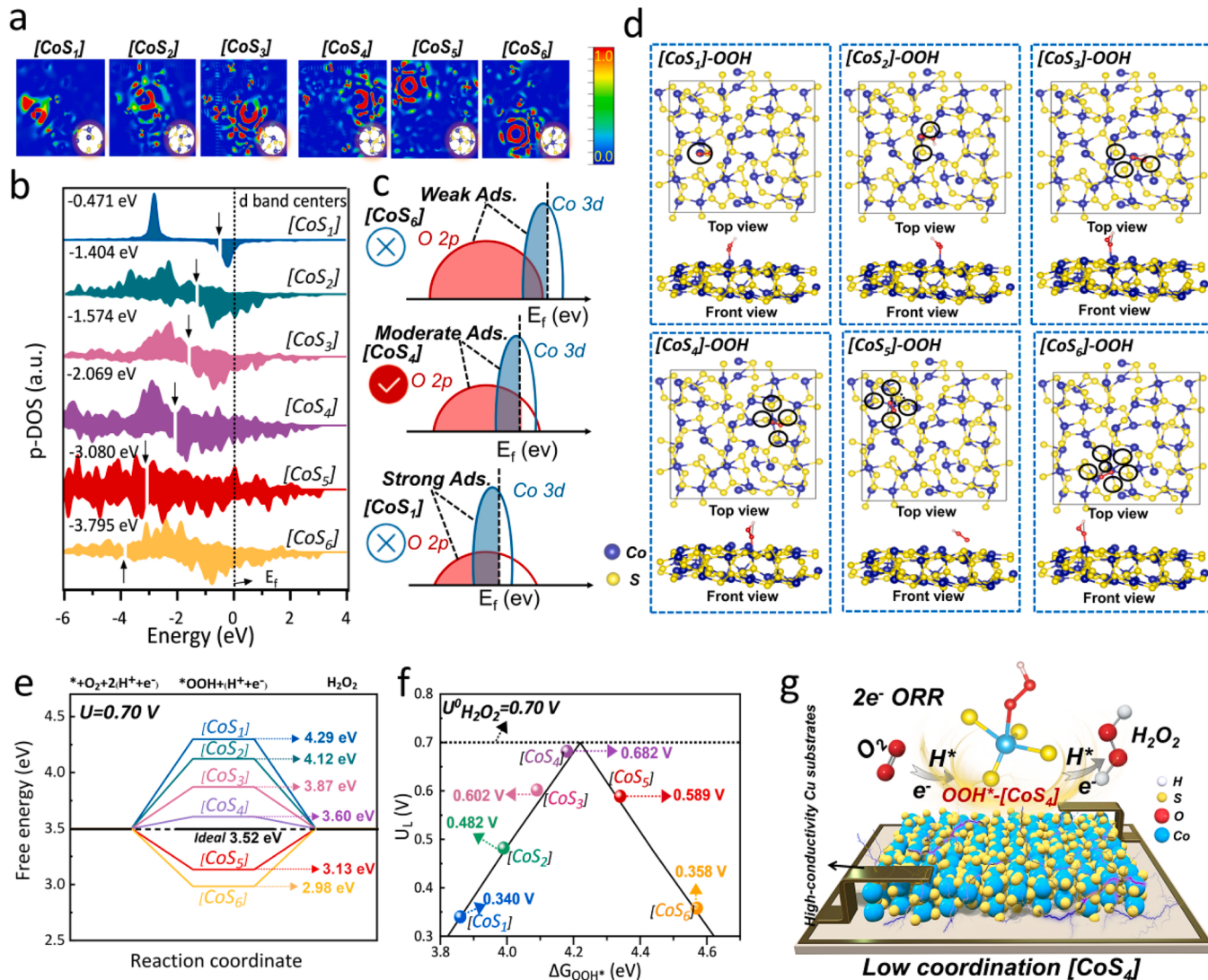


**Fig. 4.** (a) Electronic localization function (ELF) of  $\text{CoSx}$  ( $x = 1, 2, 3, 4, 5$ , and  $6$ ). (b) D-band center of as-proposed models  $[\text{CoSx}]$ . (c) Schematic diagram of  $\text{CoSx}$  ( $x = 1, 4$ , and  $6$ ) energy structure bands. (d) \*OOH adsorption model on  $\text{CoSx}$  atomic configurations and black line box marks the active site (Dark blue and yellow spheres denote Co atoms and S atoms, respectively. Black circles mark the active sites). (e) Free energy diagram of 2e<sup>-</sup> ORR on all  $\text{CoSx}$  models at 0.70 V. (f) 2e<sup>-</sup> ORR activity volcano plot, where the horizontal dashed line is the standard redox potential for 2e<sup>-</sup> ORR at 0.70 V. (g) Schematic representation of the 2e<sup>-</sup> ORR process catalyzed by the low coordination  $[\text{CoS}_4]$ .

content in CuNW@8CoSx and the environment pH discloses the root cause. As shown in Fig. 3 h,  $\text{Co}^{2+}$  is thermodynamically stable at 0.1 V, which accounts for its durability even after undergoing a long-term run [59]. Taken as a whole, the above findings clarify that the CuNW@8CoSx enables a desirable trade-off between  $4\text{e}^-$  ORR and  $2\text{e}^-$  ORR by showing exceptional stability and  $\text{H}_2\text{O}_2$  selectivity.

### 3.4. Theoretical calculation of free energy of adsorption ( $\Delta G_{\text{OOH}}$ ) and limiting potential ( $U_L$ ) of ORR reaction

To shed light on the effect of the electronic properties of CoSx on affecting the evolution of  $\text{H}_2\text{O}_2$ , DFT calculations were performed. Considering the amorphous nature of CoSx, the initial ordered model was heat-treated (The temperature is 300 K in this work) via AIMD (ab initio molecular dynamics) to disrupt its atomic arrangement and coordination states. After several rounds of optimization, the model reaches its lowest energy state and all atoms are completely relaxed and optimized. Finally, a disordered amorphous configuration containing several coordination structures including  $\text{CoS}_1$ ,  $\text{CoS}_2$ ,  $\text{CoS}_3$ ,  $\text{CoS}_4$ ,  $\text{CoS}_5$ , and  $\text{CoS}_6$  was obtained (Fig. S17). Displayed as the charge density differences and electronic localization function (ELF) in Fig. S18 and Fig. 4a, as the number of S atoms bound to the Co atom increases, the electron density around Co migrates outwards S and the polarization intensifies due to the high electronegativity of S. Namely, after Co bonds with S, continuous molecular orbitals are formed, therefore the electron localization between Co and S occurs to enable a metal-like property of CoSx [60]. Besides, CoSx is in-situ grown on Cu substrate, the CoSx shell merges with the Cu NW core to build a 1D pathway for fast electron transport, which will favor the  $2\text{e}^-$  ORR. Furthermore, the calculated Bader charge results approve the charges regarding Co and S atoms are modulated with increased S numbers in CoSx, from  $\text{CoS}_1$  to  $\text{CoS}_6$  (Table S6 and S7). In addition, all the DOS of CoSx cross the Fermi energy level ( $E_F$ ), which confirms the remarkable capability for electron transport conferred by the continuous molecular orbitals of CoSx (Fig. S19a) [60]. Fig. S19b illustrates that the p orbitals of S and the d orbitals of Co overlap, demonstrating a tight charge interaction between Co and S.

For the  $2\text{e}^-$  ORR, the strength of oxygen molecule adsorption at the active site determines the final catalytic activity. The p-band model offers an approximate description of the electronic properties and illustrates the interaction between adsorbates and metal surfaces. Based on the predicted density of states (pDOS) analysis (Fig. 4b), the p-band energy level ( $E_d$ ) of CoSx shifts downward progressively as the S atom number increases in CoSx, means increased antibonding orbitals filling, which would occupy more Co 3d orbitals and weaken the adsorption to the O 2p orbitals. It's known that the oxygen adsorption model associated with a moderate metal-oxygen bond (Fig. 4c) manifests more favorable oxygen atom reactivity and faster catalytic kinetics for  $2\text{e}^-$  ORR [61]. An overly strong metal-oxygen bond normally results in cleavage of the O-O bond, inhibiting the key intermediate  $\text{OOH}^*$  formation for the subsequent production of  $\text{H}_2\text{O}_2$ . In contrast, a weak metal-oxygen bond is unable to adsorb  $\text{O}_2$  molecules, causing inert catalytic activity. That's to say, only suitable adsorption towards oxygen can render the ideal generation of target  $\text{H}_2\text{O}_2$ . The adsorption models of  $\text{O}_2$  at different Co sites are shown in Fig. S20a and the calculated values of adsorption free energy are summarized in Fig. S20b. As expected, with minimized  $E_d$ , the adsorption energy of  $\text{O}_2$  gradually decreases from  $\text{CoS}_1$  ( $-3.134$  eV) to  $\text{CoS}_6$  ( $-0.431$  eV). Among them,  $\text{CoS}_4$  is a stable configuration with coordination by one Co and four S atoms, which tends to accept electrons from the adsorbed  $\text{H}^*$  atom and further protonation to form  $\text{OOH}^*$  while maintaining the O-O bond intact because of its moderate binding to the  $\text{O}_2$  molecule and the favorable  $E_d$  (Fig. 4c and Fig. S21).

The potential-determining step (PDS) for  $2\text{e}^-$  ORR is the transition from  $\text{OOH}^*$  to  $\text{H}_2\text{O}_2$ . As the intermediate  $\text{OOH}^*$  plays a pivotal role in producing  $\text{H}_2\text{O}_2$  molecules, the adsorption energy of  $\text{OOH}^*$  on the

electrocatalyst is a key activity descriptor of  $2\text{e}^-$  ORR during the reaction, and the theoretically optimal value of  $\Delta G_{\text{OOH}^*}$  is 4.2 eV [62]. Except that, the limiting potential ( $U_L$  in V) is usually employed as the activity metric to define the highest  $\text{H}_2\text{O}_2$  catalytic activity and zero overpotential. To reveal the important role of  $[\text{CoS}_4]$  in CuNW@CoS<sub>4</sub> for catalyzing  $2\text{e}^-$  ORR, we further added the adsorption model of  $\text{OOH}^*$  on CoSx, including  $\text{OOH-CoS}_1$ ,  $\text{OOH-CoS}_2$ ,  $\text{OOH-CoS}_3$ ,  $\text{OOH-CoS}_4$ ,  $\text{OOH-CoS}_5$ , and  $\text{OOH-CoS}_6$  (Fig. 4d). In Fig. 4e, the activity trend of CoSx is assessed based on the varied  $\text{OOH}^*$  adsorption free energy by simulating the  $2\text{e}^-$  ORR, where the optimal free energy for  $^*\text{OOH}$  adsorption is 3.52 eV. The  $^*\text{OOH}$  adsorption energy on  $\text{CoS}_1$ ,  $\text{CoS}_2$ , and  $\text{CoS}_3$  are all higher than the ideal value (3.52 eV), positively deviated by 0.77, 0.60, and 0.35 eV, respectively, representing weak adsorption of  $^*\text{OOH}$ . The  $\text{CoS}_5$ , and  $\text{CoS}_6$  deliver negative deviation in the free energies of  $-0.39$ , and  $-0.54$  eV, respectively, indicating the strong adsorption of  $^*\text{OOH}$ . When it comes to  $\text{CoS}_4$ , it exhibits the optimal deviation of the free energy, 0.08 eV, suggesting there is the best  $\text{H}_2\text{O}_2$  reaction thermodynamics. Besides that, Fig. 4 f presents the ORR volcano plot in the  $2\text{e}^-$  pathway at the 0.70 V equilibrium potential, where the maximum activity is achieved at the binding energy of  $^*\text{OOH}$  ( $\Delta G^*\text{OOH}$ ) of 4.2 eV and the thermodynamic limiting potential ( $U_L$ ) of 0.70 V. Compared with the  $\text{CoS}_1$  ( $\Delta G^*\text{OOH}$ : 3.86 eV;  $U_L$ : 0.360 V),  $\text{CoS}_2$  ( $\Delta G^*\text{OOH}$ : 3.99 eV;  $U_L$ : 0.218 V),  $\text{CoS}_3$  ( $\Delta G^*\text{OOH}$ : 4.09 eV;  $U_L$ : 0.098 V),  $\text{CoS}_5$  ( $\Delta G^*\text{OOH}$ : 4.34 eV;  $U_L$ : 0.111 V), and  $\text{CoS}_6$  ( $\Delta G^*\text{OOH}$ : 4.57 eV;  $U_L$ : 0.345 V), the  $\text{CoS}_4$  shows the superlative adsorption performance toward  $^*\text{OOH}$  ( $\Delta G^*\text{OOH}$ : 4.18 eV;  $U_L$ : 0.018 V), which lowers the reaction barrier of electrochemically reducing  $\text{O}_2$  to  $\text{H}_2\text{O}_2$  and accelerates the kinetic rate. The plausible mechanism of electrochemical  $\text{H}_2\text{O}_2$  production in low-coordination CoSx is proposed in Fig. 4 g. The  $\text{O}_2$  molecules are anchored on Co atoms in the low-coordinated  $\text{CoS}_4$  through moderate adsorption. After two SPD (Eq. (1) – (3)) steps of protonation and electron transfer,  $\text{O}_2$  first transforms in intermediate  $\text{OOH}^*$  and eventually turns into  $\text{H}_2\text{O}_2$ . Overall, the DFT results support that optimizing the Gibbs energy of  $^*\text{OOH}$  and  $E_d$  in a specific range can be realized by regulating the S numbers around Co to facilitate the electrocatalytic  $2\text{e}^-$  ORR process.

### 3.5. Electro-Fenton performance of CuNW@CoS<sub>4</sub> in degrading typical organic pollutant

On the strength of its exceptional capacity of on-site production of  $\text{H}_2\text{O}_2$ , the distinguished CuNW@CoS<sub>4</sub> electrode was applied in a dual-chamber PEM/EF reactor with  $\text{Fe}^{2+}$  involved to oxidize florfenicol (FLO), one of the representative antibiotics that is frequently detected in the ecosystem. In the reactor, the PEM serves as a barrier divider between the cathode and anode, only allowing protons to transfer during the reaction, and both  $\text{H}_2\text{O}_2$  production and contaminant removal take place at the cathode (Fig. 5a). As the degradation curves show, almost 100 % of FLO (20 ppm) is removed by the CuNW@CoS<sub>4</sub>/EF within 30 min (The initial pH of the FLO solution is 5.1, no acid is needed to pre-adjust the pH value;  $[\text{Fe}^{2+}] = 2$  mM), while that on pristine CuNW is less than 20 % (Fig. 5b). The rate constant of the CuNW@CoS<sub>4</sub>/EF system ( $0.134 \text{ min}^{-1}$ ) fitted with a pseudo-first-order kinetic model is 33.5 folds higher than that of CuNW/EF system ( $0.004 \text{ min}^{-1}$ ). Under visible light, the rate of degradation of FLO by CuNW@CoS<sub>4</sub> is negligible, thus eliminating the possibility of the effect of light on the Fenton reaction (Fig. S23a). Additionally, EPR tests (Fig. 5c) for identifying the consumption and activation of  $\text{H}_2\text{O}_2$  display that CuNW@CoS<sub>4</sub> delivers typical DMPO-•OH peaks and the signal intensity is greatly enhanced after the EF reaction starts, testifying that  $\text{H}_2\text{O}_2$  can be continuously created for activating reactive oxygen species (ROS) like hydroxyl radical (•OH). In addition, XPS was used to further analyze the active ingredients of ROS generation in CuNW@CoS<sub>4</sub>. After the EF reaction, the XPS spectra of S 2p and Co 2p demonstrate that the valence states of S and Co elements are consistent with those in the original CuNW@CoS<sub>4</sub>, which confirms the stability of the  $\text{CoS}_4$  (Fig. S22a and S22b). However,

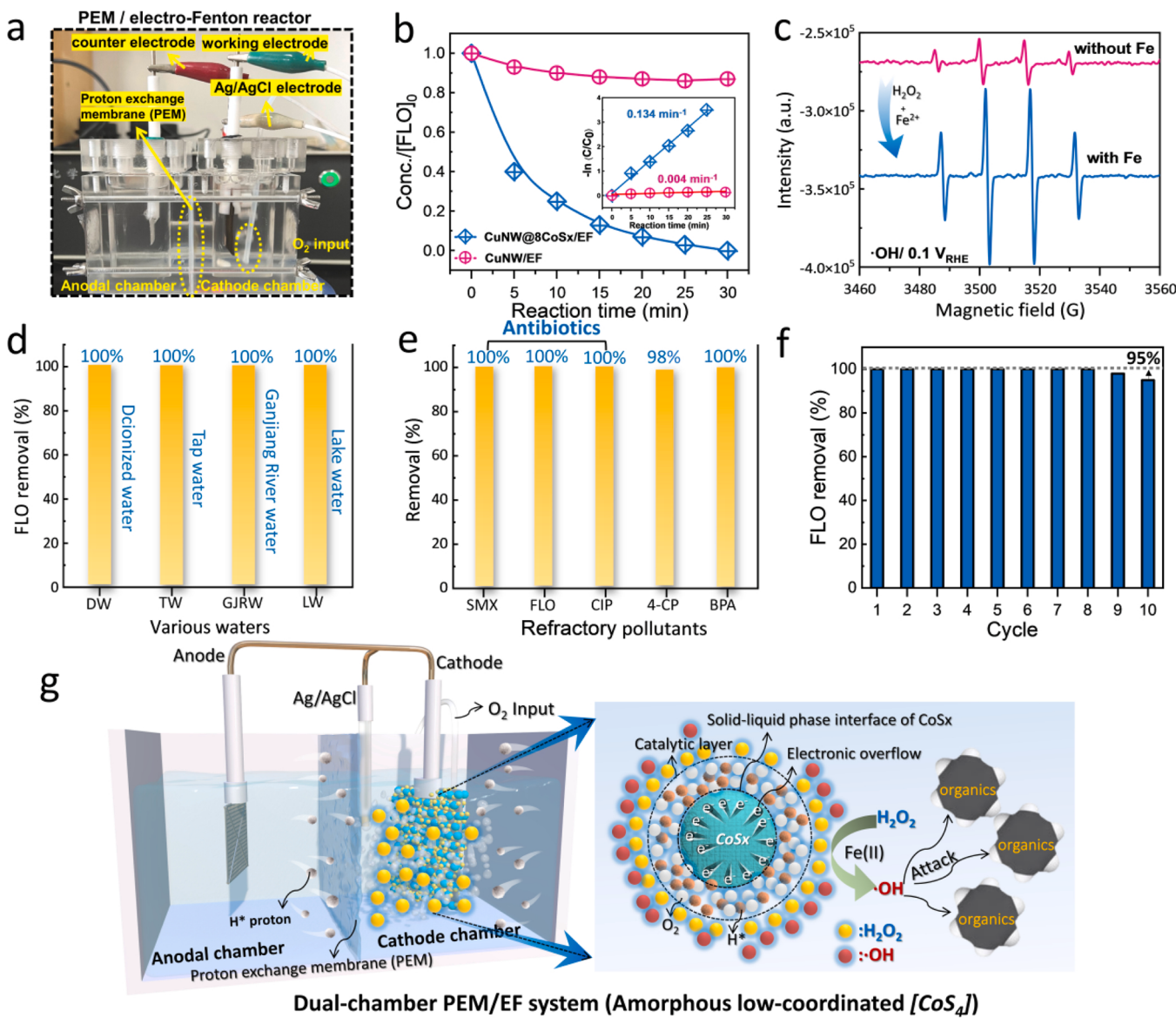
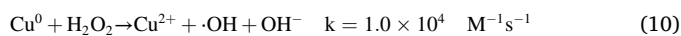


**Fig. 5.** Catalytic performance of CuNW@8CoSx as dual-chamber PEM/EF electrode. (a) Configuration of the dual-chamber PEM/EF system used for  $\text{H}_2\text{O}_2$  electrochemical synthesis and organic contaminant removal. (b) Degradation of FLO with CuNW@8CoSx/EF and CuNW/EF system. The inset shows the curves of FLO removal fitted by the pseudo-first-order reaction. (c) EPR spectra were achieved in CuNW@8CoSx/EF system, including before (without  $\text{Fe}^{2+}$ ) and during (with  $\text{Fe}^{2+}$ ) EF process. (d) The FLO degradation rates in different natural waters, (e) removal rates of various pollutants, and (f) reusability of CuNW@8CoSx-PEM/EF system for FLO degradation with deionized water background. (g) Schematic diagram of the dual-chamber PEM/EF system and involved chemical reactions.

regarding the Cu 2p XPS spectra in Fig. S22c, those characteristic peaks for  $\text{Cu}^{2+}$  at around 934.32 eV and 954.11 eV are visible, indicating the  $\text{Cu}^0$  atoms work as active ingredients in the activation of  $\text{H}_2\text{O}_2$  to form ROS via the  $\text{Cu}^0/\text{Cu}^{2+}$  transformation during the Fenton reaction (Eq. 10).



For one of the main objectives of scientific research is providing innovative solutions or techniques for practical application, the performance of CuNW@CoS<sub>4</sub>/EF system in removing FLO with actual water background was evaluated. Fig. 5d demonstrates the degradation efficiency of FLO in different natural water (i.e., Tap water, Lake water, and River water; detailed water quality parameters are listed in Table S8). The 100 % elimination regardless of the water matrix fully proves the practicability of CuNW@CoS<sub>4</sub>. The optimized system was also applied to wipe out multiple contaminants including sulfamethoxazole (SMX), florfenicol (FLO), ciprofloxacin (CIP), p-chlorophenol (4-CP), and

bisphenol A (BPA). As shown in Fig. 5e, all the contaminants are almost completely decomposed within 30 min, suggesting that CuNW@CoS<sub>4</sub>/EF is powerful to purify various organic pollutants. More importantly, the removal rate of FLO only decays by 5 % after 10 repeated runs, which makes it feasible when dealing with small-scale wastewater streams (Fig. 5f). Fig. 5g presents a schematic diagram of the double chamber PEM/EF reactor for the removal of organic pollutants and the catalytic reaction of CoSx occurring at the solid-liquid phase interface. As depicted,  $\text{H}_2\text{O}_2$  is progressively generated on CuNW@CoS<sub>4</sub> by coupling oxygen molecules, adsorbed  $\text{H}^+$ , and internal spillover electrons at the solid-liquid phase interface via the low coordination [CoS<sub>4</sub>]. In EF reaction,  $\text{Fe}^{2+}$  acts as a Fenton activator to activate  $\text{H}_2\text{O}_2$  into  $\cdot\text{OH}$  radicals for oxidizing organics ( $\text{Fe}^{2+} + \text{H}^+ + \text{H}_2\text{O}_2 \rightarrow \text{Fe}^{3+} + \text{H}_2\text{O} + \cdot\text{OH}$ ). As a result, a dual-chamber EF system that continuously generates  $\text{H}_2\text{O}_2$  and  $\cdot\text{OH}$  at the cathode was obtained, which manifests an enormous potential of CuNW@CoS<sub>4</sub> for distributed EF wastewater treatment. Fig. S23b shows the regeneration efficiency of  $\text{Fe}^{2+}$  during the

Fenton reaction. The amount of  $\text{Fe}^{2+}$  decreases promptly while the amount of  $\text{Fe}^{3+}$  soars in the first 1 min owing to the rapid consumption of  $\text{Fe}^{2+}$  in the Fenton reaction. 4 mins later, the  $\text{CuNW@CoS}_4/\text{EF}$  system demonstrates a prominent rise of  $\text{Fe}^{2+}$ , evidencing its regeneration. The total retention of  $\text{Fe}^{2+}$  slightly fluctuates around 75 % over 30 mins, indicating that the  $\text{CuNW@CoS}_4/\text{EF}$  system has good resistance to secondary iron mud pollution. Moreover, the "Ecological Structure-Activity Relationships" (ECOSAR) prediction model was further used to investigate the biological toxicity of SMX and its degradation products. The main products are formed via the typical hydroxylation pathway (Fig. S24 and Table S10). Fish, daphnia and green algae are predictors of acute (LC50) and chronic (ChV) toxicity of SMX and those intermediates. Typically, the high ecological value represents low eco-toxicity. Apparently, the intermediates produced during SMX degradation exhibit dramatic drops in the toxicity described by LC50 and ChV. The decomposition of SMX enabled by the  $\text{CuNW@CoS}_4/\text{EF}$  system follows a toxicity-diminishing process, indicating that the harm from SMX can be totally eliminated.



#### 4. Conclusions

Three-dimensional, ultrathin, amorphous low-coordination  $\text{CoS}_x$  nanosheets are in-situ grown on Cu nanowires through an ethanol-assisted electrodeposition strategy, which builds a unique "stem-leaf" shaped construction providing aligned electron-highway for ORR application. The chemical and electronic states of Co centers are well tailored by changing the S atom numbers surrounding Co with controlled deposition time. When a Co atom bond with 4 S atoms, the  $\text{Co-S}_4$  configuration can effectively optimize the d-band center of Co, making it feasible to power the  $2\text{e}^-$  ORR at a lower overpotential (0.018 V). By virtue of the highly conductive Cu support serving as a highway for transporting electrons toward  $\text{CoS}_x$  leaves, the optimal  $\text{CuNW@CoS}_4$  exhibits a 93 %  $2\text{e}^-$  ORR selectivity and 91 % Faraday efficiency in acidic media, which rivals the reported advanced ORR catalysts. When applied in a dual-chamber proton exchange membrane (PEM)/EF reactor, the  $\text{CuNW@CoS}_4$  electrode continuously supplies  $\text{H}_2\text{O}_2$  steam to oxidize the organic pollutants in contaminated water. Our findings provide constructive insights into the identification of active sites for amorphous catalysts and enlighten the design strategies for the surface engineering of highly efficient  $2\text{e}^-$  ORR electrocatalysts.

#### CRedit authorship contribution statement

**Zhenglin Chen:** Methodology, Investigation, Data curation, Visualization, Writing – original draft. **Guangzhen Liu:** Investigation, Validation. **Wenjing Cao:** Investigation. **Lixia Yang:** Conceptualization, Methodology, Writing – review & editing, Supervision, Funding acquisition. **Longshuai Zhang:** Investigation, Resources. **Shuqu Zhang:** Investigation. **Jianping Zou:** Formal analysis, Investigation. **Renjie Song:** Resources, Validation. **Wenhong Fan:** Investigation, Resources. **Shenglian Luo:** Writing – review & editing. **Dionysios D. Dionysiou:** Formal analysis, Resources, Methodology.

#### Declaration of Competing Interest

The authors declare that they have no known competing financial interests or personal relationships that could have appeared to influence the work reported in this paper.

#### Data availability

Data will be made available on request.

#### Acknowledgements

This work was supported by the National Natural Science Foundation of China (51868051, 51720105001, 51908269). We are grateful for the financial support received for this work and also acknowledge the Ekeyan Technology (Dalian) Co., Ltd. for the analysis of XAS testing and DFT calculations.

#### Appendix A. Supporting information

The Supporting Information is available free of charge at <https://pubs.acs.org/>.

Detailed description of catalysts preparation; detailed characterizations such as SEM, EPR, XPS, XRD, HR-TEM, ICP-OES, EXAFS of the catalysts; RRDE measurement details and calculation process, additional electrochemical data, additional DFT calculations data, determination of  $\text{H}_2\text{O}_2$  yield, Faraday efficiency calculations, parameters for testing contaminants by HPLC; tables for comparison of  $\text{H}_2\text{O}_2$  selectivity and overpotential with other catalysts in literature.

#### Appendix A. Supporting information

Supplementary data associated with this article can be found in the online version at [doi:10.1016/j.apcatb.2023.122825](https://doi.org/10.1016/j.apcatb.2023.122825).

#### References

- [1] S. Yang, A. Verdaguera-Casadevall, L. Arnarson, L. Silvioli, V. Colic, R. Frydendal, J. Rossmeisl, I. Chorkendorff, E.L. Stephens, Toward the decentralized electrochemical production of  $\text{H}_2\text{O}_2$ : a focus on the catalysis, *ACS Catal.* 8 (2018) 4064–4081.
- [2] E. Brillas, I. Sirés, M.A. Oturan, Electro-Fenton process and related electrochemical technologies based on Fenton's reaction chemistry, *Chem. Rev.* 109 (2009) 6570–6631.
- [3] O. US EPA, List N: Disinfectants for Use Against SARS-CoV-2, US EPA, 2020.
- [4] M. Campos, M. Jose, B. Gema Blanco, F. Jose, Hydrogen peroxide synthesis: an outlook beyond the anthraquinone process, *Angew. Chem. Int. Ed.* 45 (2006) 6962–6984.
- [5] Y. Wu, Y. Ding, X. Han, B. Li, Y. Wang, S. Dong, Q. Li, S. Dou, J. Sun, J. Sun, Modulating coordination environment of Fe single atoms for high-efficiency all-pH-tolerated  $\text{H}_2\text{O}_2$  electrochemical production, *Appl. Catal. B Environ.* 315 (2022) 121578.
- [6] Z. Lu, G. Chen, S. Siahrostami, Z. Chen, K. Liu, J. Xie, L. Liao, T. Wu, D. Lin, Y. Liu, T.F. Jaramillo, J.K. Nørskov, Y. Cui, High-efficiency oxygen reduction to hydrogen peroxide catalyzed by oxidized carbon materials, *Nat. Catal.* 1 (2018) 156–162.
- [7] K. Jiang, S. Back, A.J. Akey, C. Xia, Y.F. Hu, W.T. Liang, D. Schaa, E. Stavitski, J. K. Nørskov, S. Siahrostami, H.T. Wang, Highly selective oxygen reduction to hydrogen peroxide on transition metal single atom coordination, *Nat. Commun.* 10 (2019) 3997.
- [8] S. Chen, Z. Chen, S. Siahrostami, D. Higgins, D. Nordlund, D. Sokaras, Z. Bao, Designing boron nitride islands in carbon materials for efficient electrochemical synthesis of hydrogen peroxide, *J. Am. Chem. Soc.* 140 (2018) 7851–7859.
- [9] Z. Qiang, J. Chang, C. Huang, Electrochemical generation of hydrogen peroxide from dissolved oxygen in acidic solutions, *Water Res.* 36 (2002) 85–94.
- [10] W.T. Hess, Hydrogen Peroxide, Kirk-Othmer Encyclopedia of Chemical Technology, New York, 13 (1995) 961–995.
- [11] K.E. Ayers, L.T. Dalton, E.B. Anderson, Efficient generation of high energy density fuel from water, *ECS Trans.* 41 (2012) 27.
- [12] K. Pulidindi, H. Pandey, Hydrogen peroxide market size by end-user Industry (Paper & Pulp, Chemical, Waste Water Treatment, Mining), Industry Analysis Report, Regional Outlook, Application Potential, Price Trends, Competitive Market Share & Forecast. (2016) 2020–2026.
- [13] X. Chu, L. Zhang, Y. Li, Y. He, Y. Zhang, C. Du, N.I.R. Responsive, Doxorubicin-loaded hollow copper ferrite@ polydopamine for synergistic chemodynamic/photothermal/chemo-therapy, *Samll.* (2022), 2205414.
- [14] M.M. Montemore, M.A. Spronson, R.J. Madix, C.M. Friend,  $\text{O}_2$  activation by metal surfaces: implications for bonding and reactivity on heterogeneous catalysts, *Chem. Rev.* 118 (2017) 2816–2862.
- [15] K. Jiang, J. Zhao, H. Wang, Catalyst design for electrochemical oxygen reduction toward hydrogen peroxide, *Adv. Funct. Mater.* 30 (2020), 2003321.
- [16] B. Hammer, Y. Morikawa, J.K. Nørskov, CO chemisorption at metal surfaces and overlayers, *Phys. Rev. Lett.* 76 (1996) 2141.
- [17] V. Stamenkovic, B.S. Mun, K.J.J. Mayrhofer, P.N. Ross, N.M. Markovic, J. Rossmeisl, J. Greeley, J.K. Nørskov, Changing the activity of electrocatalysts for oxygen reduction by tuning the surface electronic structure, *Angew. Chem. Int. Ed.* 45 (2006) 2897–2901.
- [18] S. Siahrostami, A. Verdaguera-Casadevall, M. Karamad, D. Deiana, P. Malacrida, B. Wickman, M. Escudero-Escribano, E.A. Paoli, R. Frydendal, T.W. Hansen,

I. Chorkendorff, L.S. Stephens, I.E. Stephens, J. Rossmeisl, Enabling direct  $H_2O_2$  production through rational electrocatalyst design, *Nat. Mater.* 12 (2013) 1137–1143.

[19] A. Verdaguera-Casadevall, D. Deiana, M. Karamad, S. Siahrostami, P. Malacrida, T. W. Hansen, J. Rossmeisl, I. Chorkendorff, I.E.L. Stephens, Trends in the electrochemical synthesis of  $H_2O_2$ : enhancing activity and selectivity by electrocatalytic site engineering, *Nano Lett.* 14 (2014) 1603–1608.

[20] J.S. Jirkovský, I. Panas, E. Ahlberg, M. Halasa, S. Romani, D.J. Schiffirin, Single atom hot-spots at Au-Pd nanoalloys for electrocatalytic  $H_2O_2$  production, *J. Am. Chem. Soc.* 133 (2011) 19432–19441.

[21] J. Gao, H. Yang, X. Huang, S. Hung, W. Cai, C. Jia, S. Miao, H. Chen, X. Yang, Y. Huang, T. Zhang, B. Liu, Enabling direct  $H_2O_2$  production in acidic media through rational design of transition metal single atom catalyst, *Chem.* 6 (2020) 658–674.

[22] S. Sun, X. Zhou, B. Cong, W. Hong, G. Chen, Tailoring the d-band centers endows  $(Ni_x Fe_{1-x})_2P$  nanosheets with efficient oxygen evolution catalysis, *ACS Catal.* 10 (2020) 9098–9097.

[23] Q. Song, J. Li, S. Wang, J. Liu, X. Liu, L. Pang, H. Li, H. Liu, Enhanced electrocatalytic performance through body enrichment of Co-based bimetallic nanoparticles in situ embedded porous N-doped carbon spheres, *Small.* 15 (2019), 1903395.

[24] J. Chen, G. Qian, B. Chu, Z. Jiang, K. Tan, L. Luo, B. Li, S. Yin, Tuning d-band center of Pt by PtCo-PtSn heterostructure for enhanced oxygen reduction reaction performance, *Small.* 18 (2022), 2106773.

[25] G. Yang, J. Zhu, P. Yuan, Y. Hu, G. Qu, B. Lu, X. Xue, H. Yin, W. Cheng, J. Cheng, W. Xu, J. Li, J. Hu, S. Mu, J. Zhang, Regulating Fe-spin state by atomically dispersed Mn-N in Fe-NC catalysts with high oxygen reduction activity, *Nat. Commun.* 12 (2021) 1734.

[26] J. Norskov, F. Abild-Pedersen, F. Studt, T. Bligaard, Density functional theory in surface chemistry and catalysis, *Proc. Natl. Acad. Sci. India B.* 108 (2011) 937–943.

[27] B. Hammer, O.H. Nielsen, J. Norskov, Structure sensitivity in adsorption: CO interaction with stepped and reconstructed Pt surfaces, *Catal. Lett.* 46 (1997) 31–35.

[28] S. Maiti, K. Maiti, M. Curnan, K. Kim, K. Noh, J. Han, Engineering electrocatalyst nanosurfaces to enrich the activity by inducing lattice strain, *Energy Environ. Sci.* 14 (2021) 3717–3756.

[29] P.D. Tran, T.V. Tran, M. Orio, S. Torelli, Q.D. Truong, K. Nayuki, Y. Sasaki, S. Y. Chiam, R. Yi, I. Honma, J. Barber, V. Artero, Coordination polymer structure and revisited hydrogen evolution catalytic mechanism for amorphous molybdenum sulfide, *Nat. Mater.* 15 (2016) 640–646.

[30] D. Chen, C.L. Dong, Y. Zou, D. Su, Y.C. Huang, L. Tao, S. Dou, S. Shen, S. Wang, In situ evolution of highly dispersed amorphous  $CoO_x$  clusters for oxygen evolution reaction, *Nanoscale.* 9 (2017) 11969–11975.

[31] Y. Zhang, S. Deng, M. Luo, G. Pan, Y. Zeng, X. Lu, C. Ai, Q. Liu, Q. Xiong, X. Wang, Defect promoted capacity and durability of N-MnO<sub>2-x</sub> branch arrays via low-temperature NH<sub>3</sub> treatment for advanced aqueous zinc ion batteries, *Small.* 15 (2019), 1905452.

[32] N. Kornienko, J. Resasco, N. Becknell, C. Jiang, Y. Liu, K. Nie, X. Sun, J. Guo, S. R. Leone, P. Yang, Operando spectroscopic analysis of an amorphous cobalt sulfide hydrogen evolution electrocatalyst, *J. Am. Chem. Soc.* 137 (2015) 7448–7455.

[33] L. Yang, X. Wu, X. Zhu, C. He, M. Meng, Z. Gan, P.K. Chu, Amorphous nickel/cobalt tungsten sulfide electrocatalysts for high-efficiency hydrogen evolution reaction, *Appl. Surf. Sci.* 341 (2015) 149–156.

[34] J. Zhang, Y. Hu, D. Liu, Y. Yu, B. Zhang, Enhancing oxygen evolution reaction at high current densities on amorphous-like Ni–Fe–S ultrathin nanosheets via oxygen incorporation and electrochemical tuning, *Adv. Sci.* 4 (2017).

[35] S.C. Lee, J.D. Benck, C. Tsai, J. Park, A.L. Koh, F. Abild-Pedersen, T.F. Jaramillo, R. Sinclair, Chemical and phase evolution of amorphous molybdenum sulfide catalysts for electrochemical hydrogen production, *ACS Nano.* 10 (2016) 624–632.

[36] J. Wu, M. Hou, Z. Chen, W. Hao, X. Pan, H. Yang, W. Cen, Y. Liu, H. Huang, P. Menezes, Z. Kang, Composition engineering of amorphous nickel boride nanoarchitectures enabling highly efficient electrosynthesis of hydrogen peroxide, *Adv. Mater.* 34 (2022), 2202995.

[37] J. Sun, N. Guo, Z. Shao, K. Huang, Y. Li, F. He, Q. Wang, A facile strategy to construct amorphous spinel-based electrocatalysts with massive oxygen vacancies using ionic liquid dopant, *Adv. Energy Mater.* 8 (2018), 1800980.

[38] X. Zhang, Z. Luo, P. Yu, Y. Cai, Y. Du, D. Wu, S. Gao, C. Tan, Z. Li, M. Ren, T. Osipowicz, S. Chen, Z. Jiang, J. Li, Y. Huang, J. Yang, Y. Chen, C.Y. Ang, Y. Zhao, P. Wang, L. Song, X. Wu, Z. Liu, A. Borgna, H. Zhang, Lithiation-induced amorphization of Pd<sub>3</sub>P<sub>2</sub>S<sub>8</sub> for highly efficient hydrogen evolution, *Nat. Catal.* 1 (2018) 460–468.

[39] W. Yang, W. Yang, F. Zhang, G. Wang, G. Shao, Hierarchical interconnected expanded graphitic ribbons embedded with amorphous carbon: an advanced carbon nanostructure for superior lithium and sodium storage, *Small.* 14 (2018), 1802221.

[40] S. Zhang, Z. Zhang, Y. Si, B. Li, F. Deng, L. Yang, X. Liu, W. Dai, S. Luo, Gradient hydrogen migration modulated with self-adapting S vacancy in copper-doped ZnIn<sub>2</sub>S<sub>4</sub> nanosheet for photocatalytic hydrogen evolution, *ACS Nano.* 15 (2021) 15238–15248.

[41] B. Yin, X. Cao, A. Pan, Z. Luo, S. Dinesh, J. Lin, Y. Tang, S. Liang, G. Cao, Encapsulation of Co<sub>3</sub>x nanocrystals into N/S Co-doped honeycomb-like 3D porous carbon for high-performance lithium storage, *Adv. Sci.* 5 (2018), 1800829.

[42] J. Hou, Y. Sun, Y. Wu, S. Cao, L. Sun, Promoting active sites in core–shell nanowire array as Mott–Schottky electrocatalysts for efficient and stable overall water splitting, *Adv. Funct. Mater.* 28 (2018), 1704447.

[43] H. Wang, C. Tsai, D. Kong, K. Chan, F. Abild-Pedersen, J.K. Norskov, Y. Cui, Transition-metal doped edge sites in vertically aligned MoS<sub>2</sub> catalysts for enhanced hydrogen evolution, *Nano Res.* 8 (2015) 566–575.

[44] J. Wang, K. Wang, F. Wang, X. Xia, Bioinspired copper catalyst effective for both reduction and evolution of oxygen, *Nat. Commun.* 5 (1) (2014) 5285.

[45] Y. Zhang, G. Zhang, M. Zhang, X. Zhu, P. Shi, S. Wang, A. Wang, Synergistic electronic and morphological modulation by trace Ir introduction boosting oxygen evolution performance over a wide pH range, *Chem. Eng. J.* 433 (2022), 133577.

[46] T. Wu, S. Sun, J. Song, S. Xi, Y. Du, B. Chen, W.A. Sasangka, H. Liao, C.L. Gan, G. G. Scherer, L. Zeng, H. Wang, H. Li, A. Grimaud, Z.J. Xu, Iron-facilitated dynamic active-site generation on spinel CoAl<sub>2</sub>O<sub>4</sub> with self-termination of surface reconstruction for water oxidation, *Nat. Catal.* 2 (2019) 763–772.

[47] J. Liu, Y. Ji, J. Nai, X. Niu, Y. Luo, L. Guo, S. Yang, Ultrathin amorphous cobalt–vanadium hydroxide catalysts for the oxygen evolution reaction, *Energy Environ. Sci.* 11 (2018) 1736–1741.

[48] J. Wang, S. Kim, J. Liu, Y. Gao, S. Choi, J. Han, H. Shin, S. Jo, J. Kim, F. Ciucci, H. Kim, Q. Li, W. Yang, X. Long, S. Yang, S. Cho, K.H. Chae, M.G. Kim, H. Kim, J. Lim, Redirecting dynamic surface restructuring of a layered transition metal oxide catalyst for superior water oxidation, *Nat. Catal.* 4 (2021) 212–222.

[49] M. Ceotto, L. Lo Presti, G. Cappelletti, D. Meroni, F. Spadavecchia, R. Zecca, M. Leoni, P. Scardi, C.L. Bianchi, S. Ardizzone, S. Ardizzone, About the nitrogen location in nanocrystalline N-doped TiO<sub>2</sub>: combined DFT and EXAFS approach, *J. Phys. Chem. C.* 116 (2012) 1764–1771.

[50] E. Moazzeni, E.V. Timofeeva, C.U. Segre, Role of crystal lattice templating and galvanic coupling in enhanced reversible capacity of  $Ni(OH)_2/Co(OH)_2$  core–shell battery cathode, *Electrochim. Acta.* 258 (2017) 684–693.

[51] H. Funke, M. Chukalina, A. Rossberg, Wavelet analysis of extended X-ray absorption fine structure data, *Phys. Scr. T* 115 (2005) 232–234.

[52] P. Cai, J. Huang, J. Chen, Z. Wen, Oxygen-containing amorphous cobalt sulfide porous nanocubes as high-activity electrocatalysts for the oxygen evolution reaction in an alkaline/neutral medium, *Angew. Chem. Int. Ed.* 129 (2017) 4936–4939.

[53] T. Ma, S. Dai, M. Jaroniec, S. Qiao, Metal–organic framework derived hybrid Co<sub>3</sub>O<sub>4</sub>–carbon porous nanowire arrays as reversible oxygen evolution electrodes, *J. Am. Chem. Soc.* 136 (2014) 13925–13931.

[54] Y. Wu, Z. Tian, S. Yuan, Z. Qi, Y. Feng, Y. Wang, R. Huang, Y. Zhao, J. Sun, W. Zhao, W. Guo, J. Feng, J. Sun, Solar-driven self-powered alkaline seawater electrolysis via multifunctional earth-abundant heterostructures, *Chem. Eng. J.* 411 (2021), 128538.

[55] Y. Zheng, S. Hu, X.L. Zhang, H. Ju, Z. Wang, P.J. Tan, R. Wu, F.Y. Gao, T.T. Zhuang, X. Zheng, J.F. Zhu, M.R. Gao, S.H. Yu, Black phosphorous mediates surface charge redistribution of CoSe<sub>2</sub> for electrochemical  $H_2O_2$  production in acidic electrolytes, *Adv. Mater.* 34 (2022), 2205414.

[56] S. Yang, Y. Tak, J. Kim, A. Soon, H. Lee, Support effects in single-atom platinum catalysts for electrochemical oxygen reduction, *ACS Catal.* 7 (2017) 1301–1307.

[57] J. Zhang, Active sites on copper-based catalysts for electrochemical CO<sub>2</sub> reduction selectively to C<sup>2+</sup> products, *EPFL* (2022).

[58] M.R. Gao, Y. Zheng, J. Jiang, S.H. Yu, Pyrite-type nanomaterials for advanced electrocatalysis, *Acc. Chem. Res.* 50 (2017) 2194–2204.

[59] M. Li, Q. Lv, W. Si, Z. Hou, C. Huang, Sp-hybridized nitrogen as new anchoring sites of iron single atoms to boost the oxygen reduction reaction, *Angew. Chem. Int. Ed.* 61 (2022), 202208238.

[60] G. Chen, Y. An, S. Liu, F. Sun, H. Qi, H. Wu, X. Feng, Highly accessible and dense surface single metal FeN<sub>4</sub> active sites for promoting the oxygen reduction reaction, *Energy Environ. Sci.* 15 (2022) 2619–2628.

[61] C. Choi, M. Kim, H. Kwon, S. Cho, S. Yun, H. Kim, K. Mayrhofer, H. Kim, M. Choi, Tuning selectivity of electrochemical reactions by atomically dispersed platinum catalyst, *Nat. Commun.* 7 (2016) 10922.

[62] X. Zhao, Y. Wang, Y. Da, X. Wang, T. Wang, M. Xu, X. He, W. Zhou, Y. Li, J. N. Coleman, Y. Li, Selective electrochemical production of hydrogen peroxide at zigzag edges of exfoliated molybdenum telluride nanoflakes, *Natl. Sci. Rev.* 7 (2020) 1360–1366.